Journal of Engineering for Gas Turbines and Power, Volume 145, Issue 12, December 2023,
Article number 121011, Paper number GTP-23-1339
DOI:10.1115/1.4063416

Propulsion Aerodynamics for a Novel High-Speed Exhaust System

Spyros Tsentis*
Centre for Propulsion Engineering
School of Aerospace Transport and Manufacturing
Cranfield University
Bedfordshire MK43 0AL, UK
Email: Spyros.Tsentis@cranfield.ac.uk

Ioannis Goulos
Centre for Propulsion Engineering
School of Aerospace Transport and Manufacturing
Cranfield University
Bedfordshire MK43 0AL, UK
Email: i.goulos@cranfield.ac.uk

Simon Prince
Centre for Aeronautics
School of Aerospace Transport and Manufacturing
Cranfield University
Bedfordshire MK43 0AL, UK
Email: simon.prince@cranfield.ac.uk

Vassilios Pachidis
Centre for Propulsion Engineering
School of Aerospace Transport and Manufacturing
Cranfield University
Bedfordshire MK43 0AL, UK
Email: v.pachidis@cranfield.ac.uk

Vladeta Zmijanovic
Reaction Engines Ltd.
Culham Science Centre
Abingdon OX14 3DB, UK
Email: vladeta.zmijanovic@reactionengines.co.uk

ABSTRACT

A key requirement to achieve sustainable high-speed flight and efficiency improvements in space access, lies in the advanced performance of future propulsive architectures. Such concepts often feature high-speed nozzles, similar to rocket engines, but employ different configurations tailored to their mission. Additionally, they exhibit complex interaction phenomena between high-speed and separated flow regions at the base, which are not yet well understood. This paper presents a numerical investigation on the aerodynamic performance of a representative, novel exhaust system, which employs a high-speed nozzle and a complex-shaped cavity region at the base. Reynolds-Averaged Navier-Stokes computations are performed for a number of Nozzle Pressure Ratios (NPRs) and free stream Mach numbers in the range of $2.7 < NPR < 24$

*Address all correspondence to this author.

and $0.7 < M_\infty < 1.2$ respectively. The corresponding Reynolds number lies within the range of $1.06 \cdot 10^6 < Re_d < 1.28 \cdot 10^6$ based on the maximum diameter of the configuration. The impact of the cavity is revealed by direct comparison to an identical non-cavity configuration. Results show a consistent trend of increasing base drag with increasing NPR for both configurations, owing to the jet entrainment effect. Cavity is found to have no impact on the incipient separation location of the nozzle flow. At conditions of M_∞=1.2 and high NPRs, the cavity has a significant effect on the aerodynamic performance, transitioning nozzle operation to under-expanded conditions. This results in approximately 12% higher drag coefficient compared to the non-cavity case and shifts the minimum NPR required for positive gross propulsive force to higher values.

NOMENCLATURE

Roman letters

C_d Drag coefficient

C_D Nozzle discharge coefficient

$C_{V,s}$ Nozzle standard velocity coefficient

F_G Gauge stream force [N]

L Configuration total length [m]

p Static pressure [Pa]

r Radius [m]

T Static temperature [K]

y^+ Non-dimensional wall distance

Greek letters

θ, ϕ Fluid force in thrust and drag domain [N]

τ Viscous shear stress [Pa]

Dimensionless groups

Re Reynolds number

Subscripts

b Referring to the base

i Indicating location of incipient separation

w Referring to the wall

s Standard

∞ Free stream conditions

0 Total conditions

Acronyms

FSS Free Shock Separation

GCI Grid Convergence Index

GPF Gross Propulsive Force

MoC Method of Characteristics

NaN Nozzle and Nacelle configuration

NNaC Nozzle, Nacelle and Cavity configuration

RSS Restricted Shock Separation

1 INTRODUCTION

1.1 Background

High-speed propulsion has been traditionally linked to space access, launch vehicles and rocket-based transportation systems. However, there has always been an intense effort to achieve sustainable high-speed flight using air-breathing propulsion systems [1, 2, 3]. Within this context, the most common approaches include systems featuring no rotating components, which can reach high flight Mach numbers, such as Ramjets [4] and Scramjets [5]. Nevertheless, these propulsion systems do not feature the capability of generating static thrust, due to their fundamental operating principle being based on ram air compression. This has led to the advancement of combined cycle propulsion systems, including Turbine-Based [1, 6] and Rocket-Based [1, 7] combined cycle approaches (TBCC and RBCC).

Another promising technology for achieving high-speed sustainable flight is based on the concept of pre-cooled combined cycle engines. This class of engines features a heat exchanger which is incorporated to deeply cool down the incoming air prior to compression, thus extending the operational range of the downstream turbomachinery. Several concepts based on this principle have been investigated theoretically and experimentally over the years [8] and have been found to exhibit significant efficiency improvements compared to contemporary chemical rocket engines [9, 10, 11]. Studies on the conceptual development of propulsive architectures that are derived from the aforementioned pre-cooled concepts, but are tailored to sustainable high-speed flight rather than space access, have also been reported in the public domain [12].

While the efficiency advantage of these concepts is well-established from a thermodynamic point of view, their aerodynamic behavior is not yet well understood. These concepts usually feature high-speed

convergent-divergent (C-D) nozzles which are embedded at the base. This poses a major difference compared to contemporary launch vehicles, in terms of flow topology. Studies on the aerodynamic behavior of such configurations are scarce in the open literature. Additionally, in order to facilitate the overall design, cavity regions are often employed in such concepts, which could further modify their performance. During engine start-up and shut-down, the nozzle operates under highly over-expanded conditions where severe flow separation occurs, resulting in undesirable side loads. While there is a large number of studies available regarding several types of C-D nozzle flow separation for both cold [13, 14] and hot flows [14], the potential impact of a base cavity region on the flow separation has not been reported in previous studies.

1.2 Nozzle flow separation

Expanding flow within C-D nozzles is a well-established phenomenon from a fundamental perspective. Based on the ratio of nozzle static pressure at the exit over the ambient, the flow could be in over, under or ideal expansion state [15]. Under-expansion is usually less significant in terms of nozzle performance compared to over-expansion. The latter occurs at low altitudes as well as during engine start-up and shut down, and creates undesirable side loads on the nozzle walls and reduces nozzle efficiency [16, 17]. Several types of conventional C-D nozzles have been developed, each generating a specific expanding flow pattern. These include simple conical nozzles, ideal (De Laval), Truncated Ideal Contoured (TIC) [15], Thrust Optimized Contoured (TOC) [18] and Thrust Optimized Parabolic (TOP) [19] nozzles. At over-expanded conditions, the large adverse pressure gradient on the wall causes a premature flow separation upstream of the nozzle exit. The type of the contour has a significant impact on the observed flow pattern and nozzle flow separation. Two states of flow separation exist in C-D nozzles, namely, Free Shock Separation (FSS) and Restricted Shock Separation (RSS) [17]. The latter is known to appear in nozzles that feature an internal shock. At this state the flow reattaches on the nozzle walls, and transitions from FSS to RSS in an unsteady manner, significantly altering the wall pressure distribution and therefore, generating side loads [20]. Owing to the contour design of TIC nozzles, compression waves within the nozzle's divergence do not coalesce to form an internal shock, and thus, RSS is not exhibited for this type of nozzles [16, 17]. The most common shock reflection patterns that occur in all axisymmetric C-D nozzles under over-expanded conditions, are regular reflection and Mach disk reflection, while in the presence of an internal shock (e.g., for TOC nozzles), a cap-shock pattern could appear due to the impingement of the shock on the Mach disk [21].

Several well-established empirical and semi-empirical separation criteria have been developed over the years to serve as an estimation tool for the location of separation. Probably the simplest and most widely

used criterion is the one provided by Summerfield et al. [22] originally derived from studies on conical nozzles. Later on, Schmucker suggested another criterion which accounts for the inviscid Mach number at the onset of separation, and is still widely used [23]. A comprehensive review of most empirical and semi-empirical nozzle flow separation criteria can be found in [24], while a detailed comparison of their accuracy is given by Stark [14], along with his proposed criterion, which has been found to perform well for turbulent nozzle flows.

1.3 Base flow characteristics

Salient flow-field characteristics near the base and wake regions have been extensively studied in the past for generic propulsive configurations, including both planar [25] and axisymmetric ones. Most of the studies found for axisymmetric configurations deal with blunt-based bodies [26, 27, 28] and backward facing steps (BFS) [29, 30], often for power-off conditions [26, 27, 28, 31]. However, the effect of a propulsive jet on the base pressure and near-wake characteristics has also been investigated in power-on configurations [25, 29, 30]. Saile et al. [32, 33] examined the impact of the nozzle length extending from the base for a generic space launcher configuration, using an axisymmetric BFS geometry with a propulsive jet. An exceptionally excited area in the base recirculation region with distinct turbulent quantities was verified at M_∞=0.8. Statnikov et al. [34] used a hybrid zonal RANS/LES approach to investigate the wake of a cylindrical BFS, featuring an under-expanded TIC nozzle, at hypersonic speeds of M_∞=6. A subsonic cavity was formed around the step extension due to the displacement effect of the jet plume at NPR=100 and the shear layer shedding, which amplified the shear layer instability.

The effect of side boosters on such axisymmetric BFS configurations has also been investigated by Meliga and Reijasse [35]. Significant pressure drop of approximately 50% in terms of pressure coefficient at the base was observed at the presence of the boosters. Additonally, results on the side loads of more detailed configurations on the base flows of the European launchers, ARIANE5 and VEGA, can be found in the study of Schwane [36]. The geometry selection of the widely studied configurations is directly linked with the design of contemporary launch systems, where the propulsive nozzle (or nozzles) usually juts out of the vehicle base. This effect can be simplified and represented, in terms of canonical flow physics, with a BFS configuration. However, for several high-speed, combined cycle propulsion concepts, as those discussed earlier, the propulsive nozzle does not jut from the base, and therefore the BFS configuration is no longer representative. This affects the corresponding flow physics and hence, separate attention should be given to those configurations.

Base drag is a critical parameter for most propulsive architectures and is inherently connected to the near-wake flow features. It is associated with regions of separated flow at the base, and it represents the loss in pressure recovery over the base of the body [37]. Accurate evaluation of base drag is pivotal, especially for axisymmetric, blunt-based bodies, while its over-prediction can lead to substantial maximum payload capacity reduction. A characteristic case is that of the Space Shuttle program [38], where a reduction of approximately 500 kg of payload was the result of under-predicting base pressure. The effect of the jet flow on the base drag has also been investigated. It is known that aspiration or jet entrainment effect creates lower pressure region at the base and therefore increases base drag at over-expanded jet conditions. On the contrary, at highly under-expanded conditions the plume acts in favor of the base pressure and consequently, reduces base drag due to the displacement effect [37].

Several passive flow control techniques have been investigated, aiming at the reduction of base drag for bodies of revolution at the absence of a propulsive jet [39]. These are mainly associated with base geometry modifications, such as base cavities, ventilated cavities and locked vortex afterbodies, which result in increased pressure profile at the base and hence reduced base drag. Boat-tailing is another base drag reduction technique which is very simple to achieve from an engineering point of view, and has been proven successful in reducing base drag [28, 39, 40]. A comprehensive review of control mechanisms for reduction of base drag of planar and axisymmetric blunt bodies, for both power-on and power-off conditions, is given by Tanner [41], including also base-bleed, boat-tailing as well as serrated trailing edges. Additionally, increased boundary layer thickness has been found to reduce base drag [42]. Durgesh et al. [43] investigated the underlying mechanism for this phenomenon for a planar wedge and a flat plate. A decrease in the strength of the wake vortices was found for the thicker boundary layer which resulted in increased base pressure.

Base cavities in specific, have been traditionally employed for drag reduction and pressure modification at the base [39, 41]. However, their effectiveness is a function of their depth. At high ratios of cavity depth over the body's diameter, cavities have been found to have an adverse effect on base drag reduction [44]. Tripathi et al. [45], investigated the effect of base geometry modification on the control of base pressure, at both power-on and power-off conditions. They reported a notable 42% increment in base pressure coefficient at jet-off conditions for the base cavity configuration, with respect to the sharp base case, in the whole free stream Mach number range examined. In most studies including base cavities, their shape is rather simplified [41, 45] in the context of base flow control. However, modern propulsive architectures with embedded nozzles, could feature more complex cavity shapes, following the contour of the nozzle, to allow

space for nozzle gimballing and provide heat protection for critical engine components. Studies of exhaust systems employing such cavity regions have not been reported in the open literature.

1.4 Scope of present work

This paper presents a numerical investigation on the aerodynamic characteristics for a generic propulsive configuration featuring a cold flow, high-speed TIC nozzle and a complex-shaped cavity region at the base. The examined apparatus is representative of future advanced propulsion concepts, usually incorporating base-embedded cavities and C-D nozzles. The analysis employs the use of a RANS-based, compressible solver within a two-dimensional axisymmetric approach. It should be emphasised that RANS-based computations pose well-known limitations in terms of quantifying unsteady phenomena or identifying the underlying mechanisms. However, within the context of this work, this approach facilitates the understanding of the system's behavior and serves as an efficient, preemptive activity to properly accommodate the design of an on-going experimental campaign, as well as to inform future unsteady, scale-resolving computations.

The impact of free stream Mach number and NPR in terms of nozzle flow separation and overall aerodynamic characteristics is evaluated in the range of $0.7 < M_\infty < 1.2$ and $2.7 < NPR < 24$, respectively. A direct comparison against an identical, non-cavity configuration, allows the characterisation of its impact on leading performance metrics, along with identification of the underlying mechanisms. The contribution of the constituent elements comprising the total drag force is extracted through a decomposition of the aerodynamic forces that reside within the drag domain. Additionally, the effect imposed by the cavity region on the incipient location of flow separation within the nozzle is evaluated and reported. Salient flow-field features characterising each configuration are identified and support main findings from a flow physics perspective. To the authors' best knowledge, the overall aerodynamic behavior of high-speed exhaust systems featuring a propulsive nozzle embedded at the base along with a complex-shaped cavity region, has not been investigated in previous studies.

2 METHODOLOGY

2.1 Investigated Propulsive Configurations

Figure 1 presents the two propulsive configurations that are investigated numerically in this study. They both comprise of an identical axisymmetric nacelle surface, which is formed by the main cylindrical body and an ogive-shaped nose. A high-speed TIC nozzle is employed at the base. However, the configuration

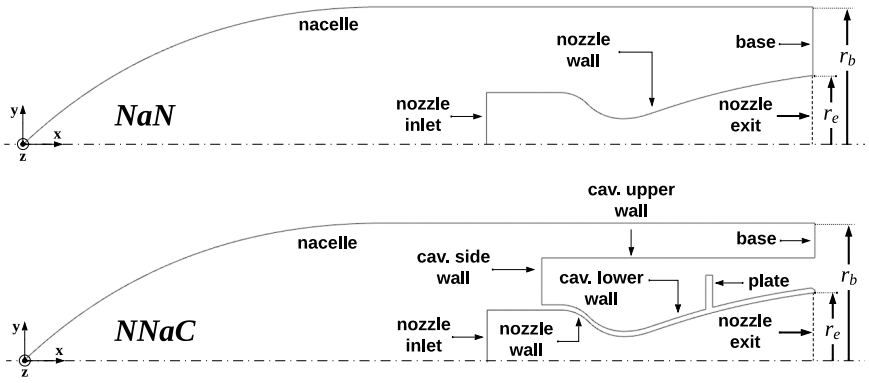

Fig. 1: Configurations under investigation: Nozzle and nacelle (top), Nozzle, nacelle and cavity (bottom)

at the bottom of Fig. 1 also features an axisymmetric cavity region located between the nacelle and the nozzle. This allows for a direct comparison between the two and therefore, conclusions can be drawn regarding the impact of the cavity region on the aerodynamic characteristics of this specific architecture. The two configurations are referred to as NaN (Nozzle and Nacelle) and NNaC (Nozzle, Nacelle and Cavity) respectively throughout the rest of this study, in line with the schematic shown in Fig. 1. The wall contour of the nozzle in the divergent section, is generated using the axisymmetric Method of Characteristics (MoC) procedure [15] in order to obtain a shock-less expansion within the nozzle. The flow properties at the sonic line in the throat region are approximated by employing Sauer's small perturbation technique [46] and used as an initial-value line for the MoC procedure in the downstream supersonic flow. The resulting ideal contoured nozzle is truncated at a wall angle of 7.6 degrees, thus providing a design exit Mach number slightly lower than 3.4 and a design NPR_d of approximately 59. The cavity region of the NNaC configuration, features a complex shape, where the lower wall follows the contour profile of the nozzle, while the upper wall has a straight-line profile. The lower cavity wall also implements an attached plate, which could represent any component related to the engine operation or heat load dissipation and acts as a vortex generator in the cavity region (Fig. 1). The associated thickness of the nozzle wall and attached plate, non-dimensionalized over the nozzle exit radius r_e, is 0.075 and 0.1, respectively.

Figure 2 demonstrates the variation of NPR with free stream Mach number and nozzle inlet total pressure in the examined design space. The exact operating conditions in terms of M_∞ and p_0 that were investigated numerically in this study are indicated with white circles, while the minimum and maximum NPR examined is 2.7 and 24 respectively (Fig. 2). As observed from this figure, the NPR in the context of this study is regulated by changing the inlet total pressure of the nozzle for fixed M_∞. This facilitates the design space exploration and de-risking activity of an on-going experimental campaign which was initiated

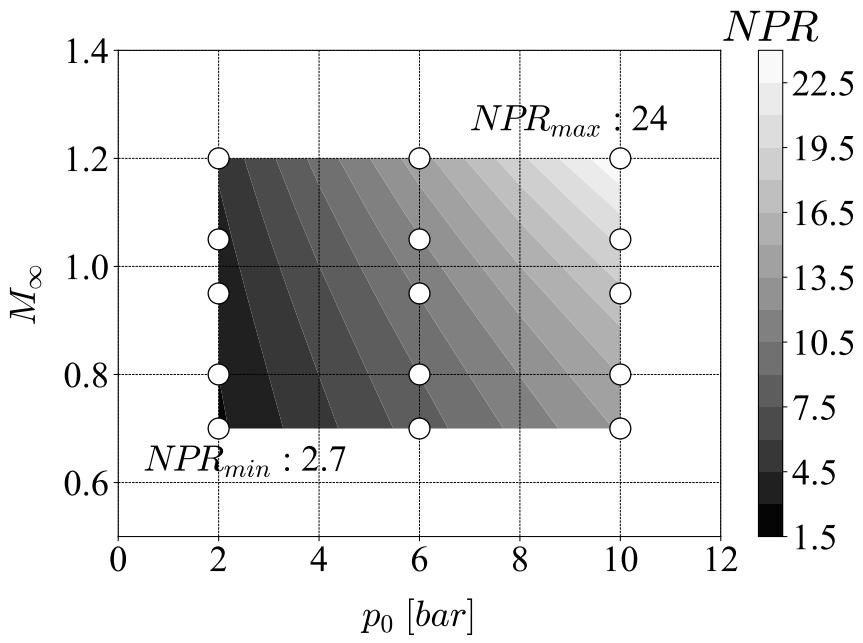

Fig. 2: NPR variation with M_∞ and p_0; White circles denote the test cases

based on the findings of this study. The nozzle is expected to operate under over-expanded conditions for the vast majority of the test cases examined. A combination of 5 different free stream Mach numbers (M_∞=0.7, 0.8, 0.95, 1.05, 1.2) and 3 nozzle inlet total pressures (p_0=2, 6 and 10 bar) were examined, producing a total number of 30 investigated cases; 15 for each corresponding configuration.

2.2 Performance accounting

A performance accounting system must be established to accommodate the proper evaluation of the aerodynamic characteristics of the investigated configurations. This also facilitates a direct comparison between the two architectures and therefore, the assessment of the impact of the cavity. Figure 3 illustrates the thrust and drag accounting method employed in this study, which is based on a well-established thrust-drag book-keeping system [47], as well as the corresponding nomenclature that is used. A near-field approach is selected, to allow direct access on the constituent elements of total forces and therefore, to identify the impact of the cavity region. The aerodynamic forces exerted on the wall surfaces by the fluid flow that lie in the drag and thrust domains are denoted by the symbols ϕ and θ respectively. These are obtained through numerical integration of the terms defining the gauge static pressure and shear-stress along the viscous surfaces (Eq. (1)). The mass flow rates as well as the gauge stream forces at the nozzle inlet and outlet are evaluated through numerical integration at the corresponding boundaries as described in Eq. (2):

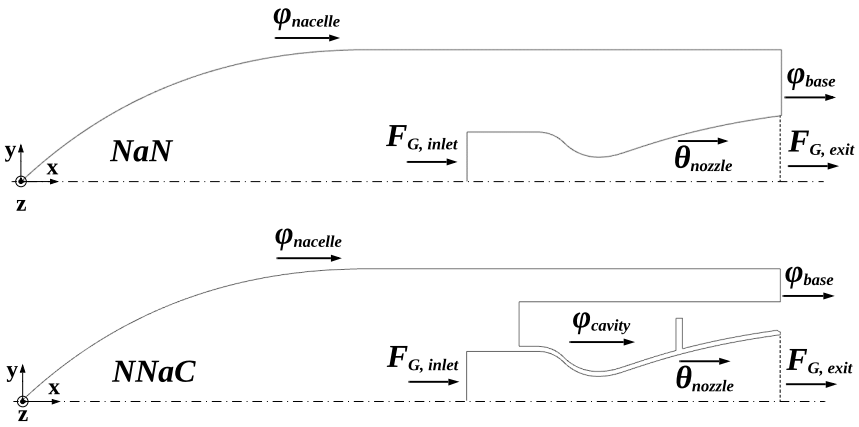

Fig. 3: Thrust and drag accounting system for the investigated configurations

$$\theta,\ \phi = \iint_S (p - p_\infty) \sin a \; dS + \iint_S t_w \cos a \; dS \tag{1}$$

$$F_G^x = \iint_{Area} \rho u_x^2 dA + \iint_{Area} (p - p_\infty) dA \tag{2}$$

In Eq. (1), p and τ_w refer to the local static pressure and shear stress respectively, p_∞ is the ambient static pressure, a is the local surface angle measured from the axial direction and dS is the elemental surface area. In Eq. (2), ρ is the density, u_x is the axial velocity component and dA is the elemental surface area of the corresponding boundary.

The aerodynamic performance of the exhaust nozzle is evaluated through the investigation of the standard velocity coefficient $C_{V,s}$. This coefficient represents the ratio of the calculated standard gross thrust $F_{G,s}$, divided by the ideal thrust, the latter being the thrust produced by the propulsive nozzle under isentropic, fully-expanded flow conditions. The definition of velocity coefficient is shown in Eq. (3). Standard gross thrust is the gauge stream force at the exit station of the nozzle and is described in Eq. (4) based

on control volume theory, while the term V_{ideal} in Eq. (3), refers to the ideal jet exit velocity that would be achieved under isentropic flow expansion to the ambient static pressure and is defined as shown in Eq. (5).

$$C_{V,s} = \frac{F_{G,s}}{\dot{m}_{actual}\, V_{ideal}} \tag{3}$$

$$F_{G,s} = F_{G,inlet} - \theta_{nozzle} \tag{4}$$

$$V_{ideal} = \sqrt{\frac{2\gamma R T_0}{(\gamma - 1)} \left(1 - \left(\frac{1}{NPR}\right)^{\frac{\gamma-1}{\gamma}}\right)} \tag{5}$$

In the above equation (Eq. (5)), NPR is the nozzle inlet total to ambient static pressure ratio, R is the gas constant, γ is the ratio of specific heats and T_0 is the total temperature at the nozzle inlet. The nozzle discharge flow coefficient, C_D is not examined herein, since the nozzle operates under choked conditions for all of the investigated cases (Fig. 2). The summation of aerodynamic forces exerted on the walls by the fluid which reside within the drag domain constitute the total modified drag force [47]. This is expressed as follows, for each configuration (Fig. 3):

$$D^*_{NaN} = (\phi_{base} + \phi_{nacelle})_{NaN} \tag{6}$$

$$D^*_{NNaC} = (\phi_{base} + \phi_{nacelle} + \phi_{cavity})_{NNaC} \tag{7}$$

The gross propulsive force, GPF is the overall aerodynamic force component in the free-stream flow direc-

tion which is produced by the exhaust system and can be obtained as:

$$GPF = F_{G,s} - D^* \tag{8}$$

This allows for the overall aerodynamic performance to take into account the region of separated flow within the nozzle under highly over-expanded conditions. Additionally, the cavity region is expected to modify the pressure at which the nozzle expands. Therefore, the impact of the cavity region on the flow separation is also investigated. This is facilitated through the identification of the incipient separation location, which is the point on the nozzle wall with the lowest pressure p_i, or where the wall pressure profile deviates from the vacuum pressure profile [14]. This point corresponds to the location where the interaction initiates and not to the actual location where the flow separates from the nozzle walls, which can be identified as the location where the wall shear stress becomes zero.

2.3 Computational methods and approach

A semicircular domain with a diameter equal to 100 times the total length of the configuration is employed for the numerical computations (Fig. 4). The length of the domain was examined to ensure that

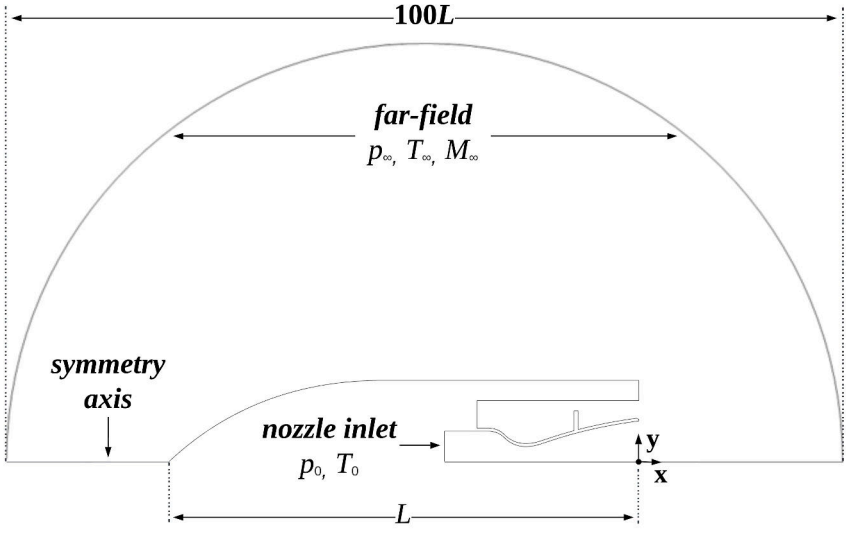

Fig. 4: Computational domain and boundary conditions

it does not affect the solution. The free stream conditions are modelled by applying a pressure far-field

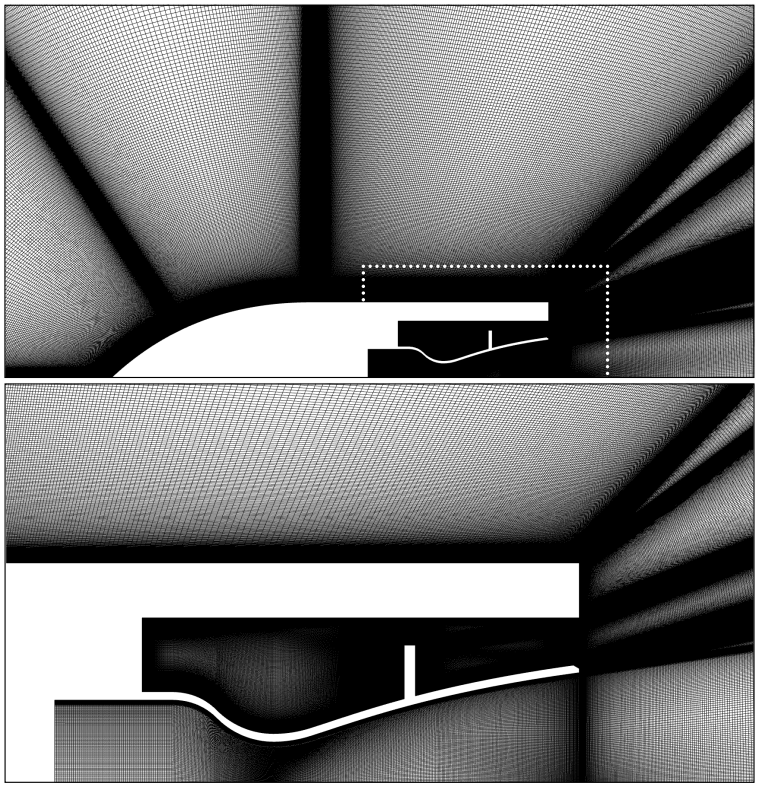

Fig. 5: Computational mesh (top) and close-up view on cavity and nozzle regions (bottom)

boundary condition (BC) on the semicircular domain, with ambient static pressure and temperature, as well as free stream Mach number as the prescribed values. The total pressure and temperature are defined at the nozzle inlet by applying a pressure inlet BC. The corresponding values of the thermodynamic parameters imposed at the boundaries are defined from the investigation of the design space of interest as shown in Fig. 2. The total temperature imposed at the nozzle inlet is 290 K. At all surfaces of the configurations, viscous no-slip and adiabatic wall BCs are applied. The domain is discretized using a multi-block, fully structured grid approach [48]. Figure 5 depicts the employed computational mesh (top), along with a close-up view in the region of the nozzle and cavity for the NNaC configuration (bottom). For the NaN configuration, not shown here for brevity, the same number of nodes as for the NNaC configuration was used, in both axial and radial directions. The resulting grid size for the NaN configuration was smaller due to the absence of the cavity region. The mesh quality in both configurations was maintained at the same level. The resulting meshes had a $y^+ < 1$ at all wall-adjacent nodes, for both configurations. A y^+ slightly higher than 1 was achieved at the base, where the boundary layer was separated for all conditions examined. Mesh adaptation to ensure a y^+ value less than 1 in the base was performed and compared to the original

Table 1: Calculation of discretization error

	ϕ = drag coefficient based on d_b (monotonic convergence)	ϕ = standard velocity coefficient (monotonic convergence)
$N1, N2, N3$	4.5M, 1.3M, 0.36M	4.5M, 1.3M, 0.36M
r_{21}	1.827	1.827
r_{32}	1.88	1.88
ϕ_1	0.8628	0.5662
ϕ_2	0.8659	0.5616
ϕ_3	0.8753	0.5501
p	1.69	1.41
ϕ_{ext}^{21}	0.8611	0.5696
e_a^{21}	0.36%	0.80%
e_{ext}^{21}	0.20%	0.59%
GCI_{fine}^{21}	0.26%	0.75%

grid. The solution in terms of performance metrics was found to be invariant to this change, and therefore, the original grid was used for this analysis, without mesh adaptation.

A grid convergence study, based on the generalized Richardson Extrapolation procedure [49], was conducted to assess the discretization error, using the second order Grid Convergence Index (GCI) [50]. Uniformly refined grids comprising of 0.36, 1.3, and 4.5 million cells were used, ensuring a grid refinement factor higher than 1.3, as recommended in [50]. A detailed summary of the results of the grid independence analysis for the NNaC configuration is shown in Table 1. The GCI corresponding to the medium mesh for the drag coefficient based on the maximum diameter of the configuration d_b, was found to be 0.26%, while the GCI for the standard velocity coefficient was 0.75%. The apparent order p, is close to the formal order of the employed discretization scheme (2^{nd}), which can be taken as an indication of the grids being in the asymptotic range [50]. Additionally, since the computed flow-field involves discontinuities (i.e., shock waves and contact surfaces) which invalidate the basis of Richardson Extrapolation, the shock location is also examined as suggested in [51]. Figure 6 shows the non-dimensional wall pressure distribution for each grid size. The wall pressure profiles for the medium and fine meshes agree within $\sim$ 0.03%, while the coarse mesh under-predicts the location of the incipient point. Therefore, based on both the GCI analysis results (Table 1) and the location of incipient separation (Fig. 6), meshes of approximately 1.3 and 1 million cells were used for the NNaC and NaN configurations respectively.

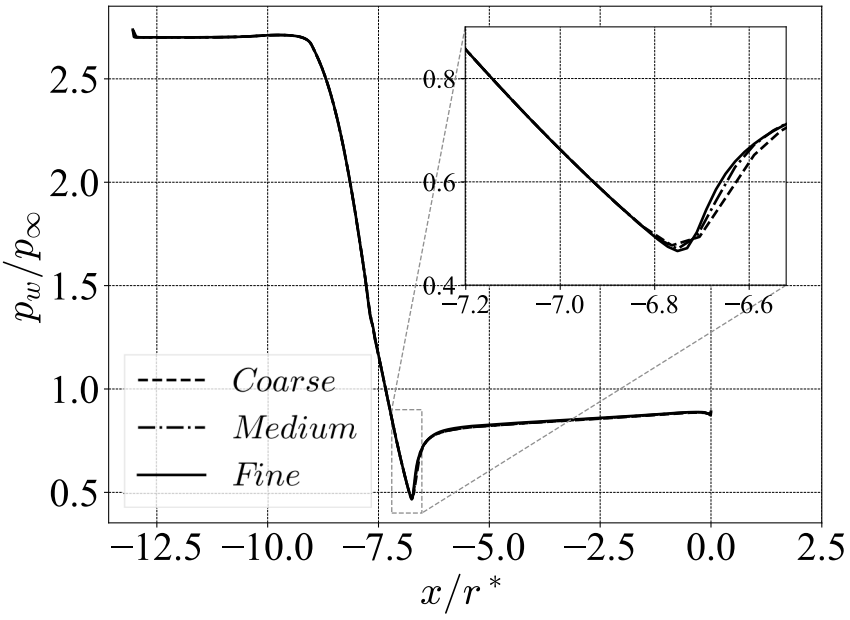

Fig. 6: Nozzle wall pressure profile for the three grids at $NPR = 2.7$ for $NNaC$

Numerical results were obtained using a two-dimensional, axisymmetric CFD approach. Computations used an implicit, density-based and compressible Reynolds-Averaged Navier-Stokes solver [52], coupled with the $k-\omega$ SST turbulence model [53]. This turbulence model has been found to perform well for over-expanded nozzle flow cases [54] as well as for powered-on, afterbody flows with separation [55]. The Roe approximate Riemann solver was employed for calculation of the convective fluxes [56]. The Green-Gauss node based method was used to calculate the flow-field gradients. A second order upwind scheme was employed for discretization of the flow primitive variables as well as for the turbulent kinetic energy k and specific dissipation rate ω. Owing to the nozzle cold flow conditions and reduced computational cost, air was modelled as an ideal-gas with thermal conductivity and specific heat capacity kept constant. The use of an 8^{th} order piecewise polynomial expression for the calculation of specific heat capacity as a function of static temperature and kinetic theory for the calculation of thermal conductivity [52], resulted in a corresponding error in GPF of $\sim$ 0.05% for the majority of the cases. The maximum error was observed at supersonic conditions of M_∞=1.2 and NPR_{max}=24 and was approximately 0.5%. Calculation of dynamic viscosity was based on Sutherland's law [57].

Due to the highly unsteady nature of the investigated flow topology, several critical performance metrics were setup to further monitor the solution convergence. For all examined cases, the metrics converged to a periodic oscillatory behavior of fixed amplitude after a large number of iterations. The amplitude cor-

responding to the GPF was below 0.1% with respect to a mean value. The resulting values are based on an averaging procedure between periodic oscillations once the amplitude was fixed. For the transonic cases of M_∞=1.05, GPF was fixed within two extreme values ($\pm 4\%$ with respect to a mean value) but exhibited non-periodic behavior due to the case being highly unsteady. This suggests that the results of a RANS-based approach for these conditions constitute the least confident ones and should be treated with caution. However, the same averaging procedure was used which allowed for major trends to be observed. An Unsteady RANS (URANS) computation was performed for these cases and the deviation in terms of average GPF was less than 0.5% with respect to the corresponding RANS result.

3 RESULTS AND DISCUSSION

3.1 Exhaust system operating conditions

Figure 7 illustrates the nozzle flow behavior across the examined design space for the NNaC configuration, in terms of the wall pressure profile. The incipient point of separation can be identified at the location where the wall pressure deviates from the ideal, full-flowing nozzle pressure profile which is included as produced by the MoC procedure [15]. The divergent section of the nozzle contour is superimposed on the results, non-dimensionalized by the throat radius (Fig. 7). This facilitates the qualitative characterization of the evolution of flow separation inside the nozzle across the investigated design space. A non-dimensional value of zero in the x-axis corresponds to the nozzle exit. For the minimum examined NPR (NPR_{min}=2.7), flow separation initiates slightly downstream of the throat, at approximately x/r^*= -6.8 as shown in Fig. 7a, thus producing a significant recirculation region inside the nozzle, which operates under highly over-expanded, FSS state. It should be noted that even the lowest NPR examined, is above critical, and therefore the flow inside the nozzle is choked throughout the whole design space for both configura-

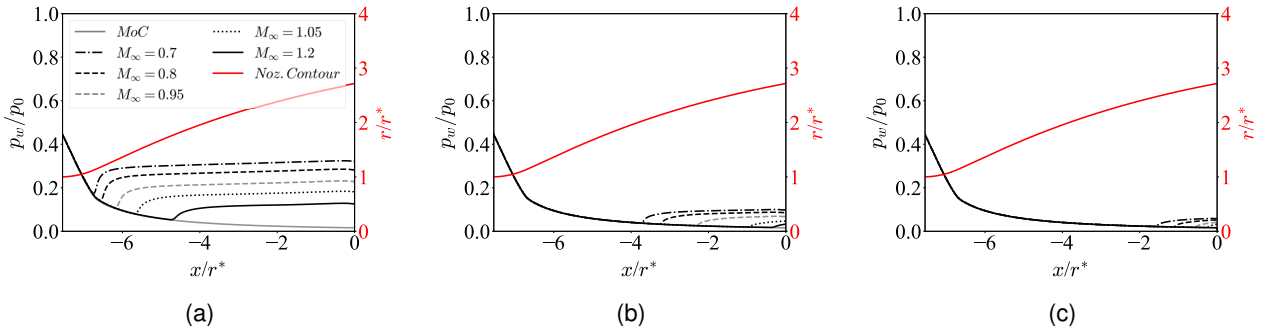

Fig. 7: Evolution of nozzle wall pressure profile with increasing M_∞ and p_0 for $NNaC$: (a) p_0=2 bar, NPR=2.7-4.8, (b) p_0=6 bar, NPR=8.2-14.4 and (c) p_0=10 bar, NPR=13.7-24

tions. Increasing M_∞ or p_0, effectively results in higher NPR and the flow can gradually withstand higher adverse pressure gradient before separation. This results in further downstream location of incipient separation as observed in Fig. 7. For the case of maximum NPR (NPR_{max}=24), which corresponds to M_∞=1.2 and p_0=10 bar, flow remains fully attached on the nozzle walls until the exit (solid black line in Fig. 7c). For all other $NPRs$ examined, flow separation initiates at some location inside the divergent section of the nozzle, therefore producing an FSS state (Fig. 7). As expected for a TIC nozzle, RSS state is not exhibited due to the absence of an internal shock [16, 17].

3.2 Aerodynamic performance across design space

The propulsive performance of both configurations across the examined design space in terms of the standard velocity coefficient, $C_{V,s}$ is shown in Figure 8. As expected, increasing the NPR for each M_∞,

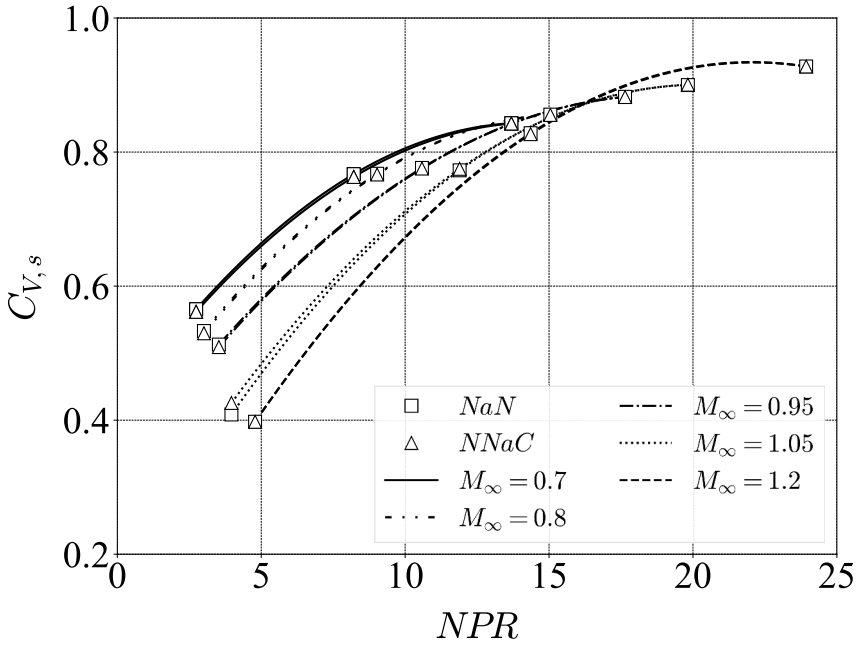

Fig. 8: Standard velocity coefficient variation with NPR and M_∞ for both configurations (curves do not represent a trend)

results in improved velocity coefficient for both configurations. This is owing to the higher expansion state that the flow can achieve with increasing NPR before the boundary layer separates from the wall due to adverse pressure gradient (Fig. 7). Additionally, NPR for fixed M_∞ is increased by regulating p_0, and therefore, maximum mass flow rate at choked conditions is higher, resulting in higher momentum flux at

the nozzle exit, hence in increased gauge stream force (Eq. 4) and improved $C_{V,s}$. For $NPRs$ below 5, a decrease in velocity coefficient with increasing M_∞ is observed. The slight increase of NPR in these cases is caused by the decrease of ambient static pressure through the regulation of M_∞, and not by changing the inlet total pressure. Therefore, the mass flow rate for these cases is the same, and the gauge stream force at the exit is dominated by the pressure recovery which reduces with increasing M_∞, in the large separated region. This effect, along with the slightly increased NPR, ergo increased ideal thrust, cause the overall velocity coefficient to drop (Eq. 3). This phenomenon is diminished, as the flow separation occurs further downstream. For the case of maximum inlet total pressure (p_0=10 bar), where flow separation is drastically reduced (Fig. 7c) and initiates close to the nozzle lip, reduction in M_∞, is translated into higher expansion and therefore higher axial jet velocity at the nozzle exit. This increases the gauge stream force (Eq. 4) and hence, the velocity coefficient. The curves connecting the results of Fig. 8 are used for visualisation reasons and should not be interpreted as depicting a trend between the data points. Such a conclusion would require further analysis for the conditions lying in between the examined cases.

Additionally, as seen in Fig. 8, it could clearly be argued that the impact of the cavity region on the velocity coefficient is negligible, with both configurations exhibiting almost identical values of $C_{V,s}$. An exception to this trend can be observed at $NPR = 4$ and M_∞=1.05, where the NNaC configuration has slightly higher velocity coefficient. If this was the manifestation of a physical mechanism, initiating as the flow transitions to the supersonic regime, it would be expected to be intensified at higher M_∞ numbers. However, for the M_∞=1.2 case, the two configurations exhibit the same velocity coefficient at NPR=4.8. Considering that at M_∞=1.05 the flow is highly unsteady, especially for low $NPRs$, the aforementioned difference in velocity coefficient could be attributed to the inability of a steady, RANS-based approach to provide highly reliable results. This difference does not invalidate the overall observed trend in case of the velocity coefficient.

Figure 9 presents the variation of drag coefficient with NPR and M_∞. C_d is based on the maximum radius of the body, that being the radius of the base, r_b as shown in Fig. 1. An obvious increase in C_d is shown with increasing NPR for all investigated free stream Mach numbers. Again, the curves connecting the values of C_d do not indicate a trend. The influence of M_∞ on drag coefficient is also depicted. A change of M_∞ from 0.7 to 0.8 has almost no effect on the overall drag coefficient. Further increase of M_∞ from 0.8 to transonic values of 0.95 and 1.05 has a significant impact on C_d, which increases by approximately 20% and 45% respectively. At the supersonic conditions of M_∞=1.2, C_d exhibits the highest value. This gradual increase of C_d through the transition from subsonic to low supersonic regimes, is typical for missile-

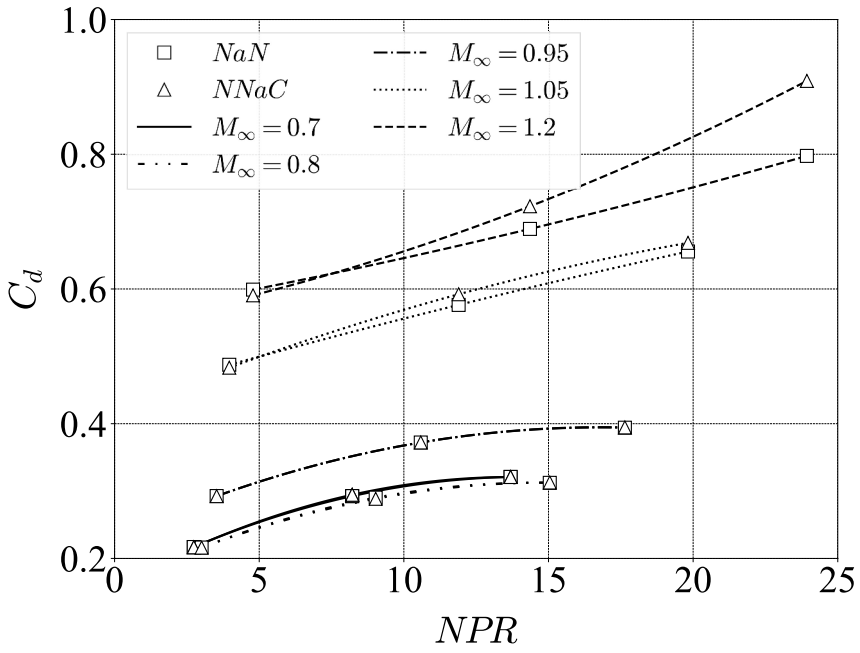

Fig. 9: Drag coefficient variation with NPR and M_∞ for both configurations (curves do not represent a trend)

shaped bodies, due to the formation of wave drag. Furthermore, it is clearly visible from Fig. 9, that the cavity region starts to significantly affect the aerodynamic forces exerted on the body as the flow enters the supersonic regime and the nozzle is not operating at very low $NPRs$. This suggests that the drag increase is driven by the jet flow conditions. At the highest NPR examined of 24, the NNaC configuration exhibits approximately 12% higher C_d value compared to the NaN configuration. This phenomenon, along with the observed trends dominating the drag domain, will be discussed in the following sections.

3.3 Decomposition of drag domain aerodynamic forces

In order to identify the underlying mechanisms of the previously exposed trends in the coefficient of drag, a decomposition of the aerodynamic forces that lie within the drag domain is performed. Throughout the rest of this study, the aerodynamic force exerted on the base of NNaC, namely ϕ_{base}^{NNaC}, represents the summation of forces exerted on the actual base and cavity regions of NNaC, as shown in the schematic of Fig. 3. This allows for a proper comparison of the base drag between the two configurations. In that manner, the total aerodynamic force that lies within the drag domain, can be decomposed into the force exerted on the nacelle and the base for both configurations. These are denoted as $\phi_{nacelle}$ and ϕ_{base} respectively, while the superscripts NaN and NNaC refer to the corresponding configuration.

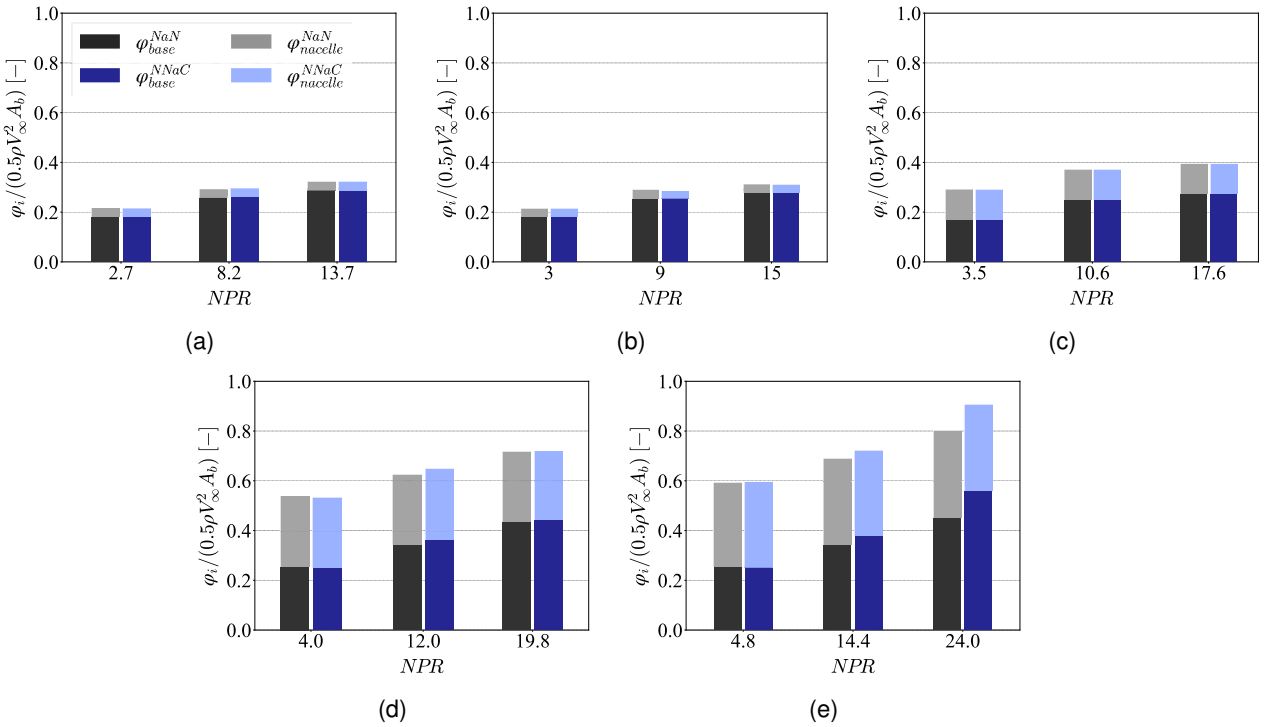

Fig. 10: Contribution of constituent elements in the overall drag coefficient across design space: (a) $M_\infty = 0.7$, (b) $M_\infty = 0.8$, (c) $M_\infty = 0.95$, (d) $M_\infty = 1.05$ and (e) $M_\infty = 1.2$

Figure 10 presents the contribution of ϕ_{base} and $\phi_{nacelle}$ in the coefficient of overall drag force with NPR and M_∞, for both NaN and NNaC configurations. As observed, the contribution of the base drag component into the overall drag force gradually increases with increasing NPR, for the whole range of M_∞ examined. For a fixed M_∞, as the NPR increases, the high-speed flow exiting the nozzle expands further (Fig. 7) and entrains the low speed, recirculating flow at the base through a turbulent mixing process, thus decreasing the base pressure. This is the so-called aspiration, or jet entrainment effect [37]. This effect becomes pronounced as the flow enters the supersonic regime, due to the lower ambient static pressure which in turn allows for further flow expansion in the nozzle, and therefore intensifies the jet entrainment process. The coefficient of drag for the NaN configuration at M_∞=1.2 is increased by a notable 33% from 0.6 to 0.8 for $NPRs$ of 4.8 and 24 respectively (Fig. 10e). This is attributed solely to the jet entrainment effect, since the contribution of the force exerted on the nacelle remains approximately the same.

Additionally, as seen in Fig. 10, the contribution of the force exerted on the nacelle on the overall drag force, increases with the free stream Mach number, while it behaves independently of the NPR. Between M_∞ of 0.7 and 0.8, nacelle contribution remains approximately unchanged (Figs. 10a and 10b). In contrast, once the flow enters the transonic regime, nacelle contribution becomes more severe, as expected due to

wave drag, with the highest being at M_∞=1.2 (Fig. 10e). Above M_∞ of 1.05, the contribution of base drag is either equal or higher compared to that of the nacelle, depending on the NPR, thus demonstrating the importance of accurate prediction of base drag for high-speed or space-access related applications. The decomposition presented in Fig. 10 clearly explains the trend of increasing C_d with increasing M_∞ and NPR observed in Fig. 9. With increasing M_∞, drag coefficient increases as a function of both nacelle and base drag. This is owing to the formation of shock waves and the lower base pressure imposed by the higher nozzle expansion (Fig. 7), which also intensifies aspiration drag. The increase of C_d with NPR for fixed M_∞, is only a function of base drag, which increases with NPR again due to the jet entrainment effect and the higher flow expansion, both lowering the pressure in the vicinity of the base, and therefore, increasing base drag.

3.4 Impact of cavity on the aerodynamic performance

Figures 10d and 10e also illustrate the effect of the cavity region on the aerodynamic behavior of the configuration. It is shown that for M_∞=1.05, the NNaC configuration exhibits slightly higher base drag compared to the NaN configuration. For M_∞=1.2, this effect is more pronounced and clearly a function of the NPR (Fig. 10e). However, this cavity effect, is not observed for the low NPR cases (i.e., $NPRs$ of 4 and 4.8 in Figs. 10d and 10e), due to the relatively early flow separation, which does not allow the jet entrainment effect to manifest within the drag domain and, therefore to influence the base pressure. As mentioned earlier, a notable increase in drag coefficient of approximately 12% is observed at the case of M_∞=1.2 and NPR_{max}=24. It is now evident based on the preceding analysis, that this increase is attributed solely to base drag.

The trends shown for the base drag components of NaN and NNaC configurations in Fig. 10 across the design space, can be further investigated by examining the base pressure of the two configurations. Figures 11a through 11e illustrate the base pressure coefficient for five points located at identical radial locations for both configurations, with M_∞ and NPR. The radial and axial locations of each point where the pressure data was taken are shown in Fig. 11f, non-dimensionalized by the throat radius, r^*. Three out of the five points for the NNaC configuration, are located on the side wall of the cavity region (Fig. 1) as shown in the bottom schematic of Fig. 11f. The employed approach of quantifying the base pressure for the two configurations is defined as such to establish consistency between numerical and on-going experimental results.

For all $NPRs$ examined in the range of M_∞=0.7-0.95, a similar behavior is observed for both configura-

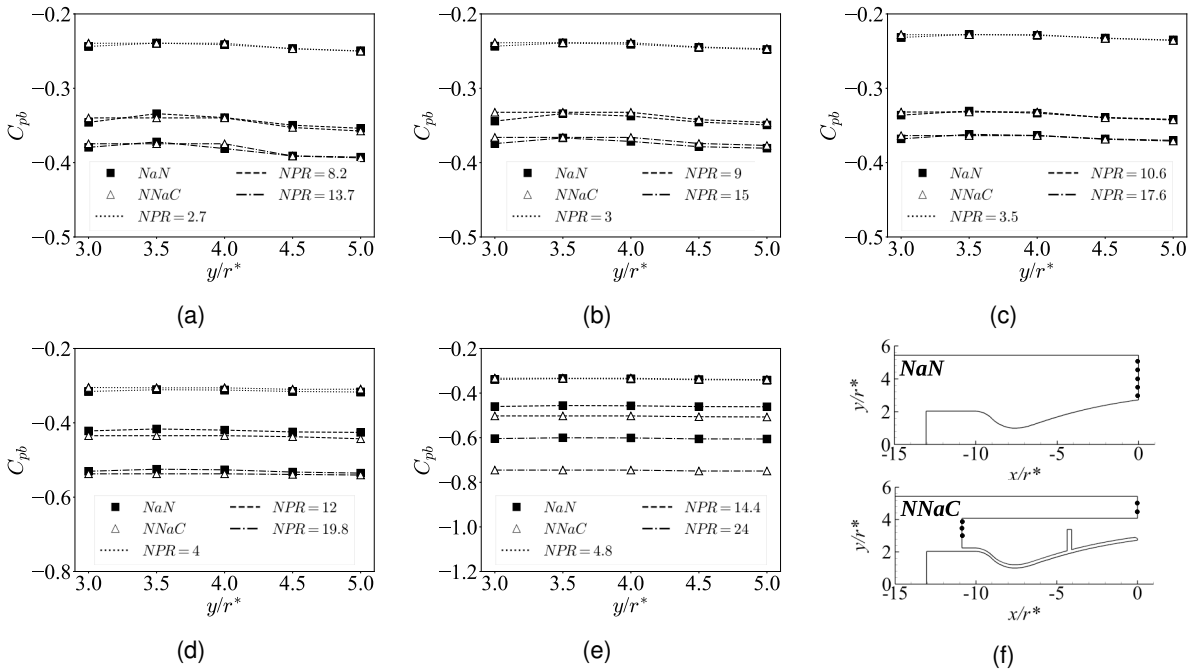

Fig. 11: Base pressure coefficient across design space for both configurations (lines do not represent a trend): (a) $M_\infty = 0.7$, (b) $M_\infty = 0.8$, (c) $M_\infty = 0.95$, (d) $M_\infty = 1.05$, (e) $M_\infty = 1.2$ and (f) location of base points

tions, where the base pressure coefficient decreases with increasing NPR, therefore increasing base drag due to aspiration effect and higher flow expansion (Figs. 11a- 11c). In these cases, C_{pb} exhibits negligible differences between the NaN and NNaC configurations. At M_∞=1.05, the NNaC configuration has slightly lower C_{pb}, for the moderate and high $NPRs$ of 12 and 19.8 respectively (Fig. 11d). This is in line with the slightly higher base drag observed in Fig. 10d. However, as mentioned earlier, this specific case is highly unsteady, especially for low $NPRs$, exhibiting non-periodic oscillatory behavior with large amplitude in the convergence metrics, and therefore the results of a RANS-based approach should be treated with caution. This means that an overall trend could potentially be captured based on averaging the solution monitoring metrics, but does not serve as a reliable case to quantify the observed differences. In contrast, at M_∞=1.2, the solution was much less challenging in terms of numerical stability for all three $NPRs$ examined. It is shown in Fig. 11e, that for the low NPR case of 4.8, base pressure is approximately the same for both configurations. This is in line with the results for base drag shown in Fig.10e for NPR=4.8. This is owing to the early flow separation which does not allow the jet flow to greatly affect the drag domain. With increasing NPR, the base pressure of the NNaC configuration is substantially decreased compared to the NaN, exhibiting a difference of almost 20% at the highest examined NPR case of 24. It should be noted that

the lower wall of the cavity (Fig. 1) systematically produced a small thrust component across the design space due to the vortex generator. This slightly decreased the contribution of the cavity in the total drag force. However, the results shown herein consider the cavity as a whole entity to allow identification of major trends and establish consistency with experimental studies.

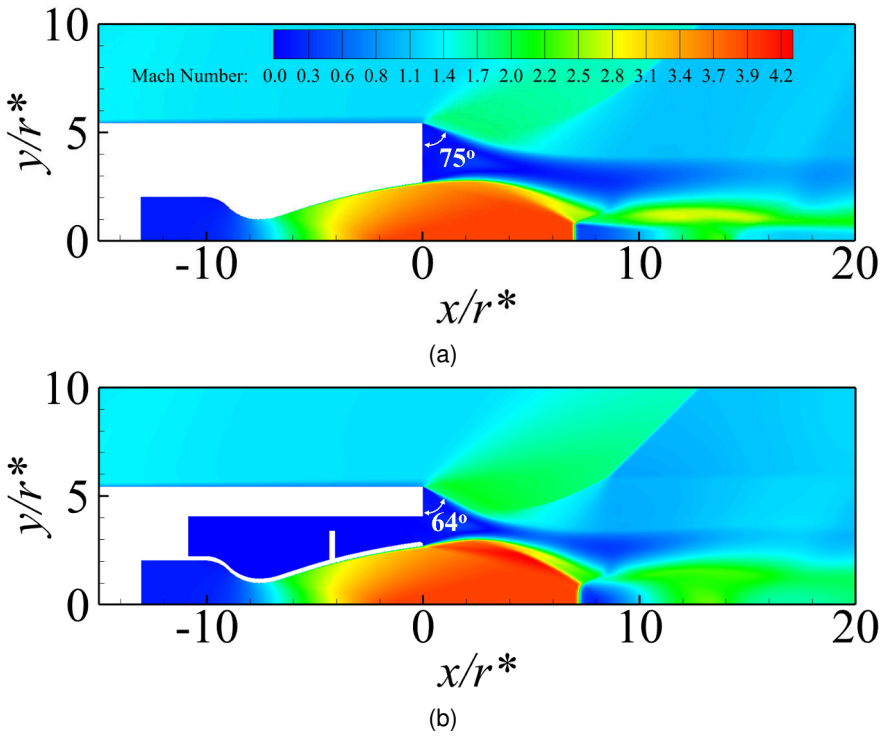

Fig. 12: Distribution of Mach number at conditions of M_∞=1.2 and NPR_{max}=24: (a) NaN and (b) $NNaC$

The analysis of base pressure results, clearly shows that the impact of the cavity region on the aerodynamic characteristics of the configuration, is a function of both the free stream Mach number and NPR. Further information on the reasons why the increase in base drag is pronounced specifically at M_∞=1.2 and NPR of 24 (approximately 12% as opposed to 4.5% at NPR=14.4), can be extracted by examining the distribution of Mach number at the base and near-wake regions for both configurations. This is depicted in Fig. 12a for the NaN and Fig. 12b for the NNaC respectively. Observing the flow-field of the two propulsive configurations, a major difference in the organisation of the flow can be identified. The cavity region in the case of NNaC, reduces the base pressure at which both the free stream and jet flow expand. This results in a more intense, steeper expansion fan which coalesces into a stronger compression shock. This is clearly visible in Fig. 12, where the flow expansion angles have been annotated, and show a reduction

of 11 degrees (from approximately 75 to 64 for NaN and NNaC respectively) in the case of the NNaC, as a result of the lower pressure imposed by the cavity. Also, both configurations produce recirculating flow with lower-than-ambient pressure at the base. This changes the effective NPR, which is defined as the nozzle inlet total pressure divided by the static pressure at which the nozzle flow expands, rather than the ambient. In the case of NaN, the effective NPR is close to the NPR_d of 59, thus producing a full flowing nozzle, with a wall pressure profile that matches the ideal one produced by the MoC procedure, not shown here for brevity. The existence of the cavity region, alters the base pressure and further increases the effective NPR, transitioning the nozzle into under-expanded operating conditions. This is evident by the further expansion of the flow after exiting the nozzle in Fig. 12b, which exhibits a barrel shock-Mach disk pattern, usually found in under-expanded nozzle flows. Both the expansion fan and the jet flow, entrain the recirculating region at the base, significantly reducing its width compared to the NaN configuration, and therefore, intensifying the aspiration effect, resulting in lower base pressure as shown in Fig. 11e.

3.5 Overall aerodynamic performance

Figure 13 presents the variation of gross propulsive force GPF, non-dimensionalized over the maximum, across the examined design space for each configuration. The investigated cases are indicated

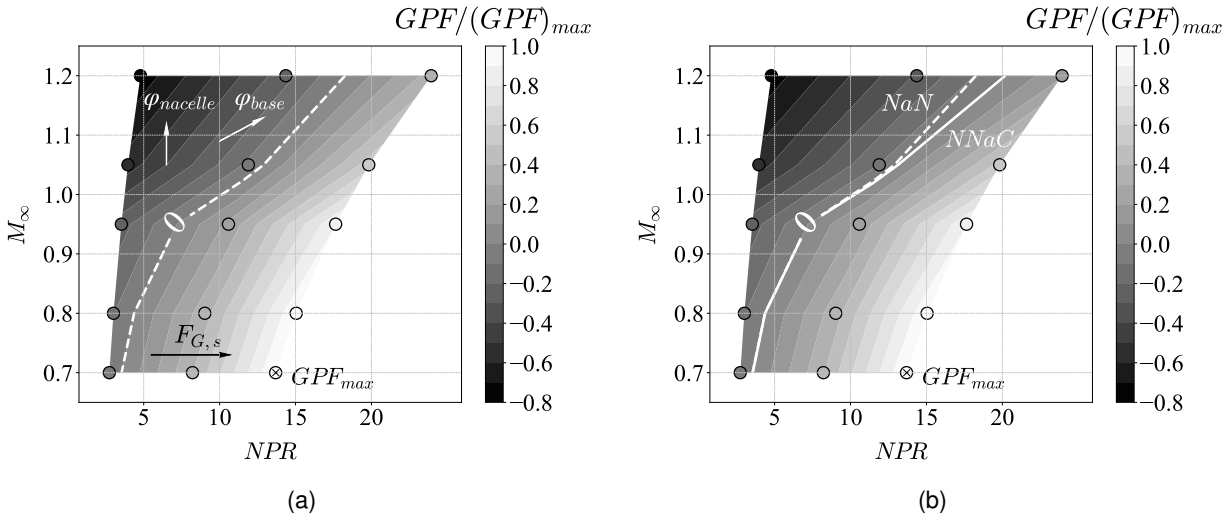

Fig. 13: Variation of Gross Propulsive Force with NPR and M_∞ across design space: (a) NaN and (b) $NNaC$

with circles of varying color according to the non-dimensional metric value $GPF/(GPF)_{max}$. Annotated in the figure is also the isoline corresponding to zero GPF, separating the regions where the overall force is

negative and positive. GPF accounts for the separated region in the nozzle at over-expanded conditions (Eq. 8). It is clearly visible that with increasing M_∞ for fixed $NPRs$, GPF decreases due to the increase in the aerodynamic force exerted on the nacelle surface, $\phi_{nacelle}$ (Fig. 13a). While NPR increases, both the standard gross thrust and base drag increase. This results in a region where drag forces are dominant as M_∞ approaches the supersonic regime (1.1-1.2) at low to medium $NPRs$ (5-15). At M_∞ <0.8, even for low $NPRs$, the GPF is positive due to the drag forces being low. The maximum GPF, denoted with the x mark in the figure, is achieved at the lowest M_∞ of 0.7 and the highest corresponding NPR examined of 13.7. Therefore, GPF_{max} is not reached at the highest investigated NPR (NPR_{max}=24) as could be expected. This is owing to the drag increase with increasing M_∞. It is emphasised here that NPR in this study is altered through the regulation of nozzle inlet total pressure p_0 for fixed M_∞. In other words, both NPR=13.7 at M_∞=0.7 and NPR_{max}=24 at M_∞=1.2, correspond to a nozzle inlet total pressure of p_0=10 bar (Fig. 2). The same trends apply for the NNaC configuration as shown in Fig. 13b. However, the impact of the cavity is clearly visible and starts to affect the performance as the flow enters the supersonic regime at medium $NPRs$ of approximately 13. As observed, the existence of the cavity region shifts the minimum $NPRs$ for which GPF becomes positive to higher values due to increased base drag. This means that the overall performance as a function of NPR would be over-predicted at specific M_∞ if the cavity region is not accounted for. This demonstrates that base-embedded cavity regions, which would be essential for nozzle gimballing and engine operation of future propulsive architectures, could notably affect the overall performance of the exhaust system under investigation.

3.6 Impact of cavity on the nozzle flow separation

Figure 14 shows the axial location of incipient separation as a function of NPR across the whole design space (Fig. 2) for both NaN and NNaC configurations. The incipient separation locations are normalized over the throat radius of the nozzle, r^*. The symbol shape defines the free stream Mach number, while the color defines the configuration, with black and red symbols referring to the NaN and NNaC respectively. Repetitive symbols correspond to higher $NPRs$ for fixed M_∞, regulated by higher nozzle inlet total pressure in line with the examined design space definition in Fig. 2. An almost-linear correlation between incipient separation location and NPR can be seen. As NPR increases and separation initiates closer to the nozzle exit, the slope of the observed trend becomes less steep. This behavior is in line with previous observations for TIC nozzles under sea-level operation [58]. The trend observed in Fig. 14 breaks for the NPR_{max} points, annotated in the graph and shown in full color, due to the flow being fully attached to the nozzle walls. This

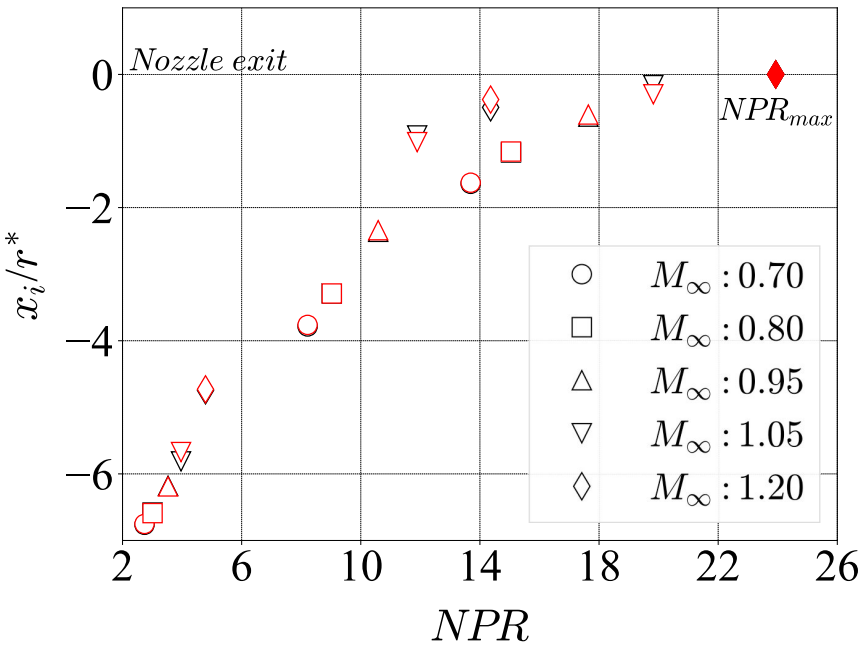

Fig. 14: Location of incipient separation as a function of NPR

is indicated by the location of lowest pressure, the latter being exactly at the nozzle exit (x_i/r^*=0) for both configurations. It is clearly obvious that the cavity region has almost no effect on the nozzle flow separation across the whole design space. This is not particularly true for the M_∞=1.05 case, where small deviations between the two configurations can be observed in Fig. 14. This is in contrast with all other cases examined and considered a numerical artifact due to the case being highly unsteady and very challenging for a RANS-based approach to produce reliable results.

Figure 15 depicts the ratio of the pressure of incipient separation p_i, over the ambient static, as a function of the corresponding wall Mach number M_i, across the design space for both NaN and NNaC. The wall Mach number is defined based on the isentropic relation for the associated ratio p_0/p_i. The same visualisation approach described for Fig. 14 applies also in Fig. 15. Superimposed on the results are several widely-used empirical and semi-empirical separation criteria. More specifically, included are the most simple and widely-used criterion by Summerfield et al. [22], the criterion suggested by Schmucker [23] as well as the one proposed by Stark [14] which is considered the state-of-the-art. An expected trend, typical for FSS state in C-D nozzles is shown in Fig. 15. Again, no impact of the cavity region on the nozzle flow separation can be identified. The M_∞=1.05 case (red and black down-pointing triangles in Fig. 15) is the only case exhibiting slight deviations between the two configurations, in line with the observations shown in Fig. 14.

Additionally, the criterion by Summerfield can be used as a rapid separation estimation tool but clearly

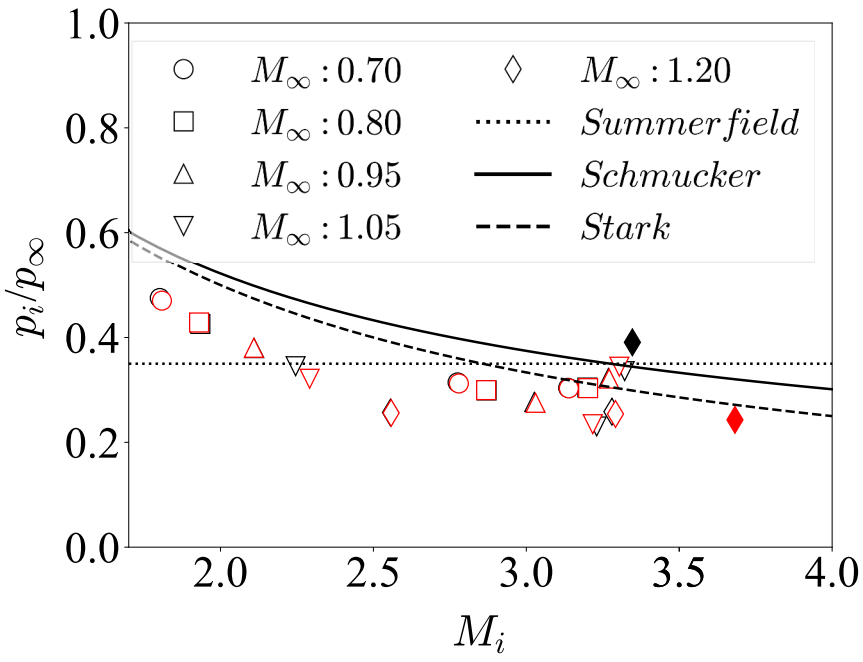

Fig. 15: Pressure of incipient separation as a function of wall Mach number

cannot be relied upon for accurate flow separation prediction, owing to its simplicity. As wall Mach number increases above approximately 2.5, the criterion suggested by Stark predicts reasonably well flow separation in this specific case, and serves as an improvement over the one proposed by Schmucker. Also, it performs better in capturing the trend of flow separation. Taking into account that many parameters influence the location of separation, including chamber temperature and the ratio of specific heats, among others, the included criteria provide reasonably good results. Furthermore, the criterion proposed by Stark, has been found to perform well above wall Mach numbers of 2.4 and for high chamber pressures [58], which does not particularly hold in this specific analysis. The fully-colored black and red diamonds in Fig. 15 correspond to fully attached flow. These data points demonstrate the different operation of the nozzle at M_∞=1.2 and NPR_{max}=24, identified earlier. The NNaC configuration (red diamond) clearly showing increased wall Mach number and lower pressure, indicating much higher expansion compared to the NaN case (black diamond), due to the flow being at under-expanded state.

3.7 Recirculating flow region inside the nozzle

At conditions of M_∞=0.7 and NPR=8.2, a recirculating region was identified immediately downstream of the Mach disk, as shown in Fig. 16a. At this NPR, the Mack disk is located within the nozzle and appears significantly bent. This generates vorticity in the downstream subsonic region which causes a rotational flow

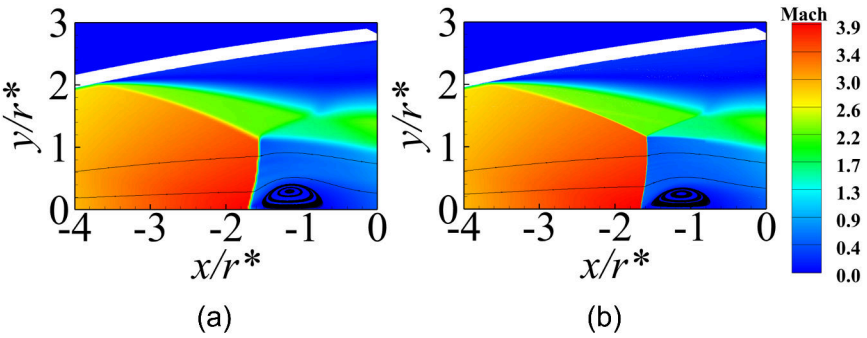

Fig. 16: Impact of grid refinement on recirculation region: (a) original grid and (b) locally refined grid

to form. The bending of the Mach disk itself is owing to upstream flow non-uniformities, in terms of radial pressure gradient within the supersonic expanding region of the flow. This is described in detail by Nasuti and Onofri in [17] as "inviscid flow separation". On the contrary, Stark and Hagemann in [59], include numerical studies where gradual grid refinement in the region of the recirculation, decreases the curvature of the Mach disk until eventually the vortex breaks up, and therefore, conclude that this phenomenon is purely a numerical artifact and a function of the grid size. In this study, a systematic local mesh refinement activity was performed for the case featuring this phenomenon on the original grid, gradually increasing the number of cells in this region. The finest grid examined comprised of 3 million cells (Fig. 16b), introduced locally in the jet shock-cell pattern. As can be seen in Fig. 16b, although the local grid refinement decreased slightly the curvature of the Mach disk, the recirculating region did not break. More recently, Martelli et al. [60], performed an experimentally validated Delayed Detached Eddy Simulation (DDES), on a highly over-expanded, sub-scale TIC nozzle. The unsteady numerical results revealed a counter-rotating vortex pair, immediately downstream of the Mach disk, in line with what Nasuti and Onofri described in [17] and with the results shown in Fig. 16. Experimental validation of this effect would be challenging, since in most cases the recirculation forms when the Mach disk is located inside the nozzle.

4 CONCLUSIONS AND FUTURE WORK

A numerical investigation of the aerodynamic characteristics for a generic, high-speed exhaust system, featuring a complex-shaped cavity and a TIC nozzle at the base is presented in this study. A two-dimensional, axisymmetric CFD approach was employed based on Reynolds-Averaged Navier-Stokes computations. Main objectives of the present analysis were to characterize the aerodynamic and propulsive behavior of the configuration, which is considered representative of future exhaust systems of advanced

propulsion concepts with embedded nozzles at the base. Additionally, of specific interest is the impact of the cavity region located between the nacelle and the nozzle. This is facilitated through the analysis of an identical, non-cavity configuration.

Results show that both investigated configurations behave similarly in terms of standard velocity coefficient, across the whole design space of M_∞ and $NPRs$ examined. Total drag coefficient is found to increase with both M_∞ and NPR. A decomposition of the aerodynamic forces within the drag domain revealed that with increasing M_∞, the forces exerted on the nacelle increase due to entering the transonic regime. Increase in NPR, by regulating the nozzle inlet total pressure, results in higher flow expansion, and therefore higher velocity in the jet boundary. This intensifies the entrainment of the separated base flow, further reducing the base pressure, ergo increasing the base drag. This was supported by examining the base pressure coefficient at different radial locations.

The cavity region is found to have almost no impact on the location of incipient separation within the nozzle flow. However, its impact on the overall aerodynamic performance is significant at low supersonic speeds and high $NPRs$. It is found that the lower base pressure imposed by the existence of the cavity region transitions the nozzle operation into the under-expanded state compared to the non-cavity configuration at M_∞=1.2 and NPR=24. Also the lower base pressure allows for a stronger flow expansion at the sharp edge formed between the nacelle shoulder and the base. The under-expanded jet along with the higher expanded air flow decrease the base pressure substantially compared to the non-cavity configuration. As a result of this effect, the cavity configuration exhibits 12% higher drag coefficient compared to the non-cavity case. Additionally, due to this phenomenon, the minimum NPR for which the exhaust system produces positive gross propulsive force is shifted to higher values for transonic and low supersonic speeds (1.05$< M_\infty <$1.2). This demonstrates that base-embedded cavity regions, which will be necessary for future propulsive architectures featuring embedded nozzles or co-planar, separate-jet, exhaust systems, could significantly affect the overall aerodynamic behavior at specific operating conditions, and therefore, should be taken into consideration early on in the design.

The results of this study, led to the initiation and design of an on-going experimental campaign to allow for higher fidelity analyses to be performed. Three-dimensional, scale resolving numerical simulations will be employed in future work alongside with the experiments, to investigate the behavior of this representative, high-speed exhaust system in an unsteady manner.

ACKNOWLEDGEMENTS

The authors would like to express their gratitude to Reaction Engines Ltd. and the Cranfield Air and Space Propulsion Institute (CASPI) for funding this project and for granting permission to publish this research.

REFERENCES

[1] McClinton, C. R., 2007, "High speed/hypersonic aircraft propulsion technology development," In *Advances on propulsion technology for high-speed aircraft. Educational Notes RTO-EN-AVT-150*, Vol. 1. NATO RTO, Neuilly-sur-Seine, France, pp. 1–32.

[2] Sziroczak, D., and Smith, H., 2016, "A review of design issues specific to hypersonic flight vehicles," *Progress in Aerospace Sciences,* **84**, pp. 1–28.

[3] Varvill, R., and Bond, A., 2003, "A comparison of propulsion concepts for ssto reusable launchers," *Journal of the British Interplanetary Society,* **56**, pp. 108–117.

[4] Ingenito, A., 2021, *Subsonic Combustion Ramjet Design* Springer Nature, Switcherland.

[5] Murthy, S., and Curran, E., 2001, *Scramjet Propulsion* AIAA.

[6] Bogar, T., Eiswirth, E., Couch, L., Hunt, J., and McClinton, C. "Conceptual design of a mach 10, global reach reconnaissance aircraft," In *32nd Joint Propulsion Conference and Exhibit*.

[7] Daines, R., and Segal, C., 2012, "Combined rocket and airbreathing propulsion systems for space-launch applications," *Journal of Propulsion and Power,* **14**(5), pp. 605–612.

[8] Dai, J., and Zuo, Q., 2020, "Key technologies for thermodynamic cycle of precooled engines: A review," *Acta Astronautica,* **177**, pp. 299–312.

[9] Tsentis, S., Gkoutzamanis, V., Gaitanis, A., and Kalfas, I., 2021, "Multi-platform app-embedded model for hybrid air-breathing rocket-cycle engine in hypersonic atmospheric ascent," *The Aeronautical Journal,* **125 (1291)**, pp. 1631–1653.

[10] Zhang, J., Wang, Z., and Li, Q., 2017, "Thermodynamic efficiency analysis and cycle optimization of deeply precooled combined cycle engine in the air-breathing mode," *Acta Astronautica,* **138**, pp. 394–406.

[11] Villace, V. F., and Paniagua, G., 2010, "Simulation of a combined cycle for high speed propulsion," In 48th AIAA Aerospace Sciences Meeting Including the New Horizons Forum and Aerospace Exposition, no. AIAA 2010-1125.

[12] Jivraj, F., Varvill, R., Bond, A., and Paniagua, G., 2007, "The scimitar precooled mach 5 engine," In 2nd European Conference for Aerospace Sciences, no. EUCASS.

[13] Gross, A., and Weiland, C., 2004, "Numerical simulation of separated cold gas nozzle flow," *Journal of Propulsion and Power,* **20**(075103), pp. 509–519.

[14] Stark, R. "Flow separation in rocket nozzles, a simple criteria," In 41st AIAA/ASME/SAE/ASEE Joint Propulsion Conference & Exhibit.

[15] Zucrow, M. J., and Hoffman, J. D., 1976, *Gas Dynamics* John Wiley and Sons, New York.

[16] Frey, M., and Hagemann, G. "Flow separation and side-loads in rocket nozzles," In 35th Joint Propulsion Conference & Exhibit.

[17] Nasuti, F., and Onofri, M., 2009, "Shock structure in separated nozzle flows," *Shock Waves,* **19**, pp. 229–237.

[18] Rao, G. V. R., 1958, "Exhaust nozzle contour for optimum thrust," *Journal of Jet Propulsion,* **28**(6), pp. 377–382.

[19] Rao, G. V. R., and Dang, A. L., 1960, "Approximation of optimum thrust nozzle contour," *ARS Journal,* **30**(6), p. 561.

[20] Shimizu, T., Miyajima, H., and Kodera, M., 2006, "Numerical study of restricted shock separation in a compressed truncated perfect nozzle," *AIAA Journal,* **44**(3), pp. 576–584.

[21] Hadjadj, A., and Onofri, M., 2009, "Nozzle flow separation," *Shock Waves,* **19**, pp. 163–169.

[22] Summerfield, M., Foster, C., and Swan, W., 1954, "Flow separation in overexpanded supersonic exhaust nozzles," *Jet Propulsion,* **24**(9), pp. 319–321.

[23] Schmucker, R., 1973, Flow processes in overexpanding nozzles of chemical rocket engines Report TB,-10,-14, Technical University Munich.

[24] Stark, R. "Flow separation in rocket nozzles - an overview," In 49th AIAA/ASME/SAE/ASEE Joint Propulsion Conference.

[25] Scharnowski, S., and Kähler, C., 2021, "Investigation of the base flow of a generic space launcher with dual-bell nozzle," *CEAS Space Journal,* **13**, pp. 197–216.

[26] Mariotti, A., and Buresti, G., 2013, "Experimental investigation on the influence of boundary layer thickness on the base pressure and near-wake flow features of an axisymmetric blunt-based body," *Exp Fluids,* **54**(1612).

[27] Mariotti, A., Buresti, G., and Salvetti, M. V., 2015, "Connection between base drag, separating boundary layer characteristics and wake mean recirculation length of an axisymmetric blunt-based body," *Journal of Fluids and Structures,* **55**, pp. 191–203.

[28] Tran, T., Dinh, H., and Chu, H. e. a., 2021, "Effect of boattail angle on near-wake flow and drag of axisymmetric models: a numerical approach," *J Mech Sci Technol,* **35**, pp. 563–573.

[29] Paciorri, R., Sabetta, F., Valenza, F., Fauci, R., Passaro, A., and Baccarella, D., 2013, "Base-pressure experimental investigation on a space launcher in subsonic regime," *Journal of Spacecraft and Rockets,* **50**(3), pp. 572–578.

[30] Deprés, D., Reijasse, P., and Dussauge, J. P., 2004, "Analysis of unsteadiness in afterbody transonic flows," *AIAA Journal,* **42**(12), pp. 2541–2550.

[31] Weiss, E. P., Deck, S., Robinet, J. C., and Sagaut, P., 2009, "On the dynamics of axisymmetric turbulent separating/reattaching flows," *Physics of Fluids,* **21**(075103).

[32] Saile, D., Kühl, V., and Gülhan, A., 2019, "On the subsonic near-wake of a space launcher configuration with exhaust jet," *Experiments in Fluids,* **60**(165).

[33] Saile, D., Kühl, V., and Gülhan, A., 2021, "On subsonic near-wake flows of a space launcher configuration with various base geometries," *Experiments in Fluids,* **62**(122).

[34] Statnikov, V., Sayadi, T., Meinke, M., Schmid, P., and Schröder, W., 2015, "Analysis of pressure perturbation sources on a generic space launcher after-body in supersonic flow using zonal turbulence modeling and dynamic mode decomposition," *Physics of Fluids,* **27**(016103).

[35] Meliga, P., and Reijasse, P., 2012, "Unsteady transonic flow behind an axisymmetric afterbody equipped with two boosters," In 25th AIAA Applied Aerodynamics Conference.

[36] Schwane, R., 2015, "Numerical prediction and experimental validation of unsteady loads on ariane5 and vega," *Journal of Spacecraft and Rockets,* **52**(1), pp. 54–62.

[37] Hammond, W. E., 2001, *Design Methodologies for Space Transportation Systems* AIAA, Virginia.

[38] Roberts, B. B., Wallace, R. O., and Sims, J. L., 1983, "Plume base flow simulation technology," In Shuttle Performance: Lessons Learned, part I, no. NASA-CP-2283-PT-1, pp. 1–18.

[39] Viswanath, P. R., 1996, "Flow management techniques for base and afterbody drag reduction," *Progress in Aerospace Sciences,* **32**, pp. 79–129.

[40] Viswanath, P. R., and Patil, S. R., 1990, "Effectiveness of passive devices for axisymmetric base drag reduction at mach 2," *Journal of Spacecraft and Rockets,* **27**(3), pp. 234–237.

[41] Tanner, M., 1975, "Reduction of base drag," *Progress in Aerospace Sciences,* **16**(4), pp. 369–384.

[42] Whitmore, S. A., and Naughton, J. W., 2002, "Drag reduction on blunt-based vehicles using forebody surface roughness," *Journal of Spacecraft and Rockets,* **39**(4), pp. 596–604.

[43] Durgesh, V., Naughton, J. W., and Whitmore, S. A., 2013, "Experimental investigation of base-drag reduction via boundary-layer modification," *AIAA Journal,* **51**(2), pp. 416–425.

[44] Morel, T., 1979, "Effect of base cavities on the aerodynamic drag of an axisymmetric cylinder," *Aeronautical Quarterly,* **30**, pp. 400–412.

[45] Tripathi, A., Manisankar, C., and Verma, S. B., 2015, "Control of base pressure for a boat-tailed axisymmetric afterbody via base geometry modifications," *Aerospace Science and Technology,* **45**, pp. 284–293.

[46] Sauer, R., 1947, General characteristics of the flow through nozzles at near critical speeds Memorandum No.1147, NACA, Washington, DC.

[47] MIDAP, S. G., 1979, Guide to in-flight thrust measurement of turbojets and fan engines AGARDograph No. 237, Advisory Group for Aerospace Research and Development, 7 Rue Ancelle 92200 Neuilly, Sur Seine, France.

[48] ANSYS INC., 2009, *Ansys Workbench User's Guide* 275 Technology Drive, Canonsbug, PA 15317.

[49] Richardson, L. F., and Gaunt, J. A., 1927, "The deferred approach to the limit," *Philos. Trans. R. Soc. London,* **Ser. A, 226**, pp. 307–357.

[50] Celik, I. B., Ghia, U., Roache, P. J., Freitas, C. J., Coleman, H., and Raad, P. E., 2008, "Procedure for Estimation and Reporting of Uncertainty Due to Discretization in CFD Applications," *Journal of Fluids Engineering,* **130**(7).

[51] Roache, P. J., 1998, *Verification and Validation in Computational Sciences and Engineering* Hermosa, New Mexico, USA.

[52] ANSYS INC., 2013, *Ansys Fluent Theory Guide* 275 Technology Drive, Canonsbug, PA 15317.

[53] Menter, F. R., 1994, "Two-equation eddy-viscosity turbulence models for engineering applications," *AIAA Journal,* **32**, pp. 1598–1065.

[54] Allamaprabhu, C., Raghunandan, B., and Morinigo, J., 2011, "Improved prediction of flow separation in thrust optimized parabolic nozzles with fluent," In 47th AIAA/ASME/SAE/ASEE Joint Propulsion Conference & Exhibit.

[55] Hasan, R. G. M., McGuirk, J. J., Apsley, D. D., and Leschziner, M. A., 2004, "A turbulence model study of separated 3d jet/afterbody flow," *The Aeronautical Journal,* **108**(1079), p. 1–14.

[56] Roe, P. L., 1981, "Approximate riemann solvers, parameter vectors, and difference schemes," *Journal of Computational Physics,* **43**(2), pp. 357–372.

[57] Sutherland, W., 1893, "The viscosity of gases and molecular forces," *Philos. Mag.,* **36**, pp. 507–531.

[58] Stark, R., and Wagner, B., 2008, "Experimental study of boundary layer separation in truncated ideal contour nozzles," *Shock Waves,* **19**, pp. 185–191.

[59] Stark, R., and Hagemann, G., 2007, "Current status of numerical flow prediction for separated nozzle flows," In 2nd European Conference for Aerospace Sciences, no. EUCASS.

[60] Martelli, E., Saccoccio, L., Ciottoli, P. P., Tinney, C. E., Baars, W. J., and Bernardini, M., 2020, "Flow dynamics and wall-pressure signatures in a high-reynolds-number overexpanded nozzle with free shock separation," *Journal of Fluid Mechanics,* **895**(1612), p. A29.

2023-09-13

Propulsion aerodynamics for a novel high-speed exhaust system

Tsentis, Spyros

American Society of Mechanical Engineers

Tsentis S, Goulos I, Prince S, et al., (2023) Propulsion aerodynamics for a novel high-speed exhaust system. Journal of Engineering for Gas Turbines and Power, Volume 145, Issue 12, December 2023, Article number 121011, Paper number GTP-23-1339

https://doi.org/10.1115/1.4063416